



# On the internal collapse phenomenon at the closure of cavitation bubbles in a deceleration process of underwater vertical launching

Yiwei Wang<sup>a,\*</sup>, Chenguang Huang<sup>a</sup>, Xin Fang<sup>b</sup>, Xiaocui Wu<sup>a</sup>, Tezuan Du<sup>a</sup>

<sup>a</sup> Key Laboratory for Mechanics in Fluid Solid Coupling Systems, Institute of Mechanics, Chinese Academy of Sciences, Beijing 100190, China

<sup>b</sup> The State Key Laboratory of Nonlinear Mechanics, Institute of Mechanics, Chinese Academy of Sciences, Beijing 100190, China



## ARTICLE INFO

### Article history:

Received 28 July 2015

Received in revised form

23 December 2015

Accepted 3 February 2016

Available online 3 March 2016

### Keywords:

Unsteady cavitating flow

Internal collapse

Underwater launching process

Deceleration

## ABSTRACT

In a typical experiment of underwater vertical launching, cavitation bubbles are generated in the low-pressure regions of the vehicle in the water and collapse when the projectile runs through the free surface. A new internal collapse phenomenon that advances from the tail to the head of the axisymmetric projectile has been observed in an underwater launching experiment: it differs from usual collapse phenomena and is rarely observed in water tunnel tests. During this process, cavities shrink upstream quickly, producing high impact pressure, and fast re-entry jets form, inducing strong instabilities. Analysis indicates that this phenomenon is relative to rapid changes in vehicle speed and cavitation number. Thin cavitation bubbles are generated when the vehicle accelerates rapidly, and then vapor condenses rapidly and forms an additional body force at the closure of the cavity in the deceleration process. As a result, large velocity directed to the wall to the wall is generated, and the liquid water layer continues to move toward the wall and impact as an internal collapse. Numerical simulations are also performed on the decelerating effect on the cavity evolution. Results indicate that the pressure increase is a critical factor, which results in a nonlinear change in the cavity length. In proportion to the enlargement of the deceleration, the cavities shorten more quickly.

© 2016 Elsevier Ltd. All rights reserved.

## 1. Introduction

When objects run in water at high speed, cavitations occur in low-pressure regions, where part of the liquid water changes into vapor. Cavitation is one of the most important and complicated phenomena in hydrodynamics. In particular, when cavitation bubbles collapse, high-pressure pulses are generated, exerting major impact and even causing damage on the structures of vehicles [1].

Bubble collapse has been intensively investigated theoretically, experimentally, and numerically in the past, including the dynamics of single sphere bubbles [2–5], non-sphere bubbles [6–9], and interaction among a limited number of bubbles [10–16]. However, very large scale computation involving the solution of Navier–Stokes equations is required to determine the behavior of many bubbles [17]. Simplified models of bubble clusters and bubbly flows have also been established and used to identify various mechanisms of flow behaviors [18–20].

In applied research on hydrodynamics and ocean engineering, the collapse of bubble clusters that involve a huge number of bubbles is also an important issue. For example, cavitation bubbles

collapse when vehicles are launched through the free surface of the water to open air [21], and bubble dynamics is also an important issue in research on underwater explosion [22,23]. Moreover, the instabilities at cavitation closures are usually prominent in cloud cavitations with quasi-periodical breaking-off and shedding [24,25]. Observations show that the shedding cavitation cloud may collapse at the cavitation closure, and this kind of collapse is closely related to the instability of cavitation bubbles [26–29].

Given the strongly unsteady behavior of cavitating flows, the variation in the velocity is an important influencing factor on the evolution of cavitating bubbles. Some researchers have studied the changes in the shape of natural supercavitation under various decelerating conditions using numerical methods [30–32]. Chen et al. [33] numerically and analytically investigated the development of cavitation bubbles around submerged vehicles with decelerating navigation and indicated that the cavity is induced to collapse by the deceleration after fluctuation. These aforementioned numerical results are mostly similar in terms of their qualitative characteristics. However, the associated experimental results available in the literature are very limited because of the limitations in water tunnel and other test methods. As a consequence, numerical results are also lacking in rigorous validation.

In the present study, an internal collapse is observed in a vertical underwater launch experiment without bubble shedding. The

\* Corresponding author. Tel.: +86 1082543811.

E-mail address: [wangyw@imech.ac.cn](mailto:wangyw@imech.ac.cn) (Y. Wang).

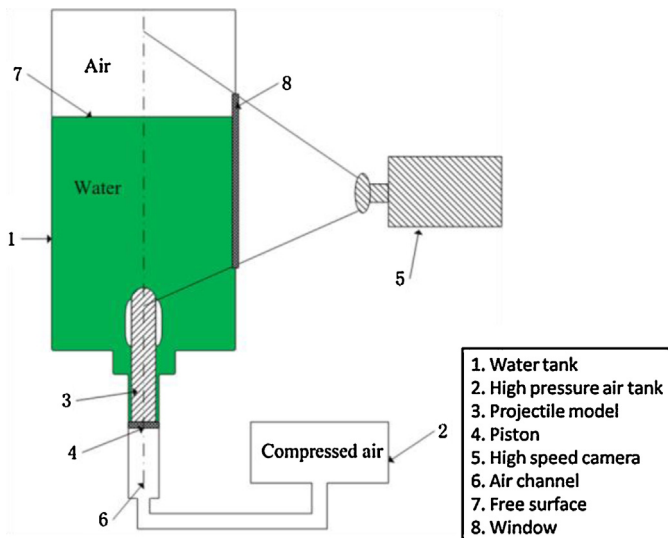


**Fig. 1.** Schematic of the experiment system.

bubble collapses at the closure and is propagated reversely and quickly upstream. The mechanisms and influence of the internal collapse are analyzed. Furthermore, numerical simulations are performed to study the effects of speed change by varying the deceleration of the projectile. The present work is organized as follows: Section 2 presents the experimental setup, numerical methods, and relevant flow parameters. Section 3 focuses on experimental observations, in which the overall evolution of the cavitation patterns in the whole launching process, the rapid cavity shortening phenomenon in the internal collapse process, and the strong re-entry jet induced by the collapse are described. Section 4 discusses the mechanism of the internal collapse. Section 4.1 identifies the fast acceleration and deceleration of the projectile as the main cause of the internal collapse, and Section 4.2 further examines the effect of deceleration on the variation of the cavity shape, along with numerical results. Section 5 summarizes the major conclusions of the study.

## 2. Experimental and numerical methods

### 2.1. Experimental setup

To investigate the underwater launch problem, a small-scale vertical underwater launch system is established, as shown in Fig. 1. The measuring equipment used includes pressure probes to obtain the air pressure after decompression by vacuum pump and temperature probes to obtain the water temperature.

In the launch experiment, the piston is pushed by compressed air and propels the projectiles to accelerate and move vertically. The cavitation bubbles generated in the low-pressure regions around the shoulder of the projectiles evolve unsteadily and collapse after exiting the water. The projectile model is hollow and made of stainless steel. The equivalent density of the model is similar to liquid

**Table 1**  
Basic launch parameters.

Water depth	1.185 m
Air pressure	40 kPa
Water temperature	19.2 °C
Fastest measured speed of projectile	21.8 m/s
Frame rate of high speed camera	6000 fps
Projectile diameter	70 mm
Projectile length	500 mm
Projectile mass	1.9 kg

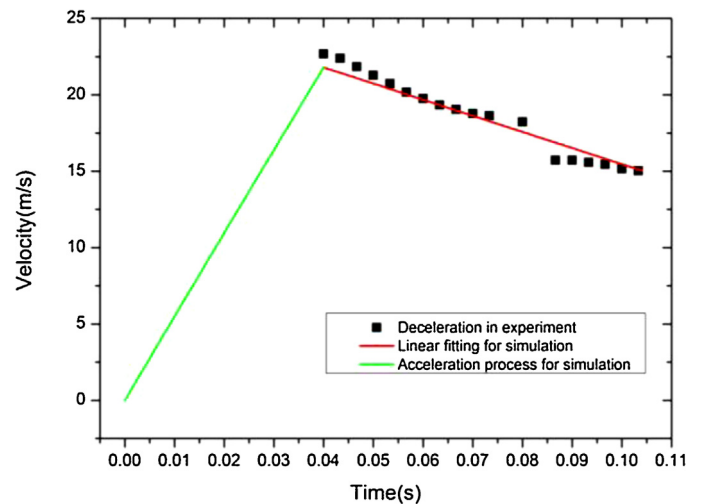


**Fig. 2.** Projectile speed in the launch process. The black solid squares represent the speed of the projectile by conducting pixel analysis on the experimental results. The red curve represents the linear fitting of the experiment results, while the green curve represents a linear estimate of the speed in the acceleration process. The speed values shown in the green and red curves are combined and used as the speed condition in the basic numerical simulation (For interpretation of the references to color in this figure legend, the reader is referred to the web version of this article.).

water to avoid the large influence of the forces of gravity and buoyancy. The basic launch conditions of the typical experiments are listed in Table 1.

The projectile speed varies throughout the whole process. In the observed part, the speed curve can be calculated as shown in Fig. 2 by image processing and is approximately linear. For the acceleration part in the launch tube, the movement of the projectile cannot be observed. Assuming that the high-pressure gas expands uniformly, the pressure on the piston surface can be conducted by the volume ratio of the gas tank and tunnel. Subsequently, the projectile speed in the accelerating process is estimated as shown in Fig. 2.

### 2.2. Numerical methods

To simulate the motions and phase change of liquid water and vapor, the mixture/multiphase flow equations are adopted based on the third type of method mentioned in Section 1. The continuity and momentum equations of the mixture of liquid water, vapor, and non-condensable air are established as

$$\frac{\partial}{\partial t}(\rho_m) + \nabla \cdot (\rho_m \vec{v}_m) = 0 \quad (1)$$

$$\begin{aligned} \frac{\partial}{\partial t}(\rho_m \vec{v}_m) + \nabla \cdot (\rho_m \vec{v}_m \vec{v}_m) \\ = -\nabla p + \nabla \cdot [(\mu_m + \mu_t)(\nabla \vec{v}_m + \nabla \vec{v}_m^T)] + \rho_m \vec{a} + \rho_m \vec{g} \end{aligned} \quad (2)$$

where  $p$  is the mixture pressure,  $\rho_m$  is the mixture density,  $\vec{v}_m$  is the mixture velocity vector, and  $\vec{g}$  is the gravitational acceleration.  $\vec{a}$  is the acceleration of the flow field and is calculated by  $\vec{a} = -\dot{\vec{v}}$ , where  $\dot{\vec{v}}$  is the acceleration of the projectile model. The laminar viscosity  $\mu_m$  is defined as the density-weighted average of the three components.  $\mu_t$  is the turbulent viscosity closed by the RNG  $k-\varepsilon$  model. The mixture density  $\rho_m$  is defined by

$$\rho_m = (1 - \alpha_v)\rho_l + \alpha_v\rho_v \quad (3)$$

where  $\alpha_v$  is the component volume fraction of vapor, and  $\rho_v$  and  $\rho_l$  are the component densities of the vapor and liquid components, respectively.

The mass fraction equation for vapor is

$$\frac{\partial(\rho_v \alpha_v)}{\partial t} + \frac{\partial(\rho_v \alpha_v u_j)}{\partial x_j} = R_e - R_c \quad (4)$$

where  $R_e$  and  $R_c$  are the evaporation and condensation rate, respectively, which can be simulated in the cavitation model established by Zwart et al. [34].

$$\begin{cases} R_e = F_{vap} \frac{3a_{nuc}(1 - \alpha_v)\rho_v}{R_B} \sqrt{\frac{2}{3} \frac{\max(p_v - p, 0)}{\rho_l}} \\ R_c = F_{cond} \frac{3\alpha_v \rho_v}{R_B} \sqrt{\frac{2}{3} \frac{\max(p - p_v, 0)}{\rho_l}} \end{cases} \quad (5)$$

where the generalized bubble radius  $R_B$  is set at  $10^{-6}$  m, the nucleation site volume fraction  $a_{nuc}$  is set to  $5 \times 10^{-4}$ , the evaporation coefficient  $F_{vap}$  is set to 50, and the condensation coefficient  $F_{cond}$  is set to 0.01.

To calculate the turbulent viscosity  $\mu_t$  in Eq. (3), the two transport equations for turbulence kinetic energy  $k$  and its dissipation rate  $\varepsilon$  are solved as the RNG  $k-\varepsilon$  model.

$$\frac{\partial}{\partial t}(\rho_m k) + \frac{\partial}{\partial x_i}(\rho_m k v_i) = \frac{\partial}{\partial x_j} \left( \alpha_k \mu_{eff} \frac{\partial k}{\partial x_j} \right) + G_k - \rho_m \varepsilon \quad (6)$$

$$\frac{\partial}{\partial t}(\rho_m \varepsilon) + \frac{\partial}{\partial x_i}(\rho_m \varepsilon v_i) = \frac{\partial}{\partial x_j} \left( \alpha_\varepsilon \mu_{eff} \frac{\partial \varepsilon}{\partial x_j} \right) + C_{1\varepsilon} \frac{\varepsilon}{k} G_k - C_{2\varepsilon} \rho_m \frac{\varepsilon^2}{k} \quad (7)$$

where  $G_k$  represents the generation of turbulence kinetic energy caused by the mean velocity gradients, calculated as  $G_k = -\rho \bar{u}_i' \bar{u}_j' \frac{\partial u_j}{\partial x_i}$ , the quantities  $\alpha_k$  and  $\alpha_\varepsilon$  are the inverse effective Prandtl number for  $k$  and  $\varepsilon$ , respectively,  $\alpha_k = \alpha_\varepsilon = 1.393$ , and the model constant is  $C_{1\varepsilon} = 1.42$ ,  $C_{2\varepsilon} = 1.68$ .

For the ordinary case, the turbulent viscosity is calculated by  $\mu_t = C_\mu \rho_m \frac{k^2}{\varepsilon}$ , which is overestimated in the mixed region [35]. As such, a modified turbulent viscosity, which is found to improve significantly the simulations of the cloud shedding, is instead defined as follows:

$$\mu_t = f(\rho) C_\mu \frac{k^2}{\varepsilon}. \quad (8)$$

where  $C_\mu = 0.0845$ , and

$$f(\rho) = \rho_v + \frac{(\rho_m - \rho_v)^n}{(\rho_l - \rho_v)^{n-1}}, \quad n = 10. \quad (9)$$

These unsteady numerical simulations are performed based on the finite volume method with the PISO scheme, using the commercial CFD software FLUENT. The equations are discretized by a second-order implicit scheme in time and a second-order upwind scheme in space. The numerical parameters are summarized in Table 2.

Given the axisymmetric characteristics of the flow field, 2D axisymmetric simulation is performed. The computational domain shown in Fig. 3 is discretized with a block-structured grid with  $240 \times 200$  cells. The height of the first layer is set to  $1/10,000$  of the projectile's diameter to ensure that  $y+$  equals 1 approximately

**Table 2**  
Numerical parameters.

Simulation type	Unsteady
Pressure–velocity coupling	PISO
Temporal scheme	2nd-order implicit
Time step	$1 \times 10^{-5}$ s
Spatial scheme	2nd-order upwind
Pressure interpolation scheme	Body force weighted
Turbulence model	Modified RNG $k-\varepsilon$

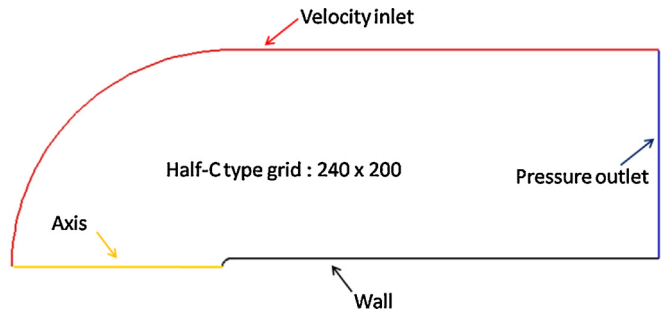


Fig. 3. Computational domain and boundary conditions.

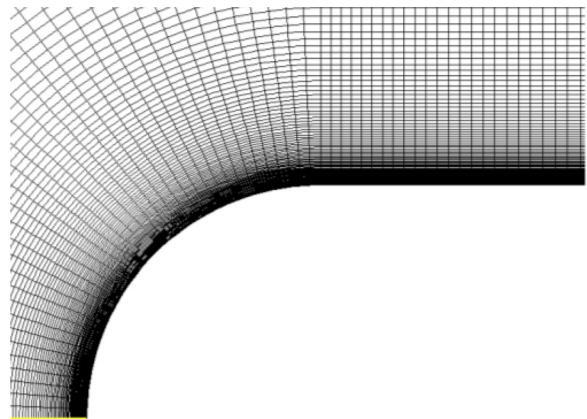


Fig. 4. Near wall grids around the head of the projectile.

(as shown in Fig. 4). Thus, the two-layer model is adopted to resolve the laminar sub-layer. Similar schemes are used to simulate underwater launching in previous works [21,36].

### 3. Evolution of the cavitation bubbles

#### 3.1. Overall evolution of the cavitation bubbles

In the two stages of cruising and exiting water, cavitation bubbles evolve as shown in Fig. 5. The whole process can be divided into two large stages according to the projectile motion. In the cruising stage, the projectile is fully submerged in the water, and the cavity grows first and then shrinks gradually without exhibiting any obvious phenomena of cavity breaking up and shedding. In the exiting stage, the projectile head moves out of the free surface, and the whole cavity collapses in a very short period.

According to the development of the cavity, the launching process is further divided into the following four small stages:

- (1) When the projectile moves at a relatively high speed, the cavity grows continuously, and the cavity shape becomes thin and long (as shown in Fig. 5(a) and (b)).
- (2) As the projectile speed decreases, the trailing edge of the cavity advances upward, and the cavity internally collapses and shortens rapidly (as shown in Fig. 5(c) and (d)).
- (3) The re-entry jet is generated during the shortening process, which is shown as the movement of the brighter white liquid water from the trailing edge to the leading edge of the cavity.
- (4) When the projectile moves through the free surface with a large cavity, the low pressure in the cavitation region cannot remain, and the cavity collapses.

The cavity growth, the re-entry jet, and the collapse in the exiting stage have been widely investigated in previous studies, but

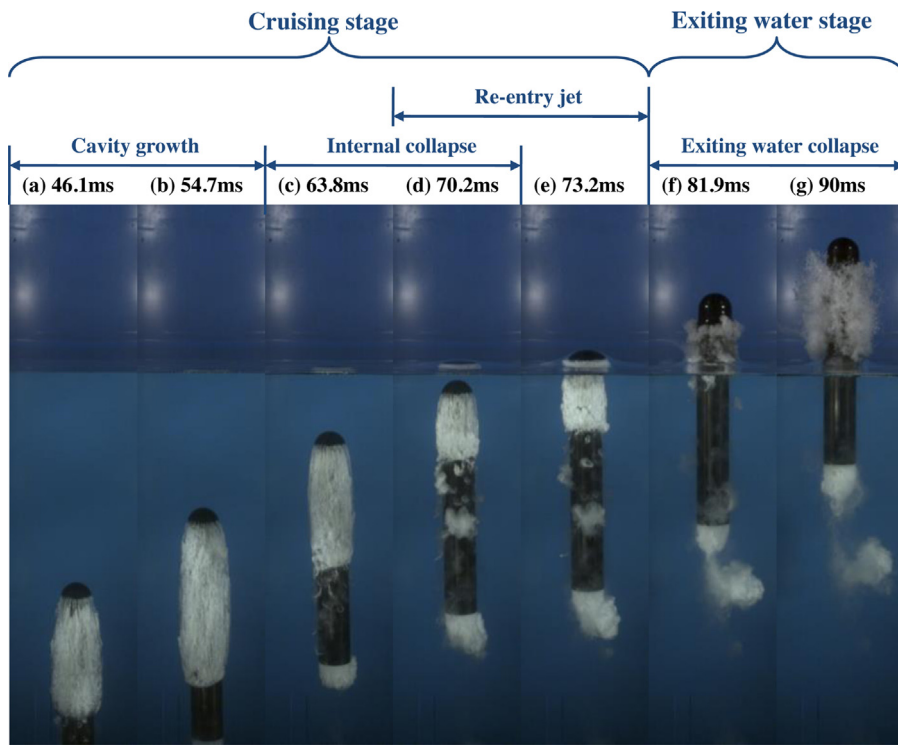


**Fig. 5.** Overall evolution of cavitation bubbles. The process is divided into two stages according to the projectile movement, which in turn is divided into two stages according to the cavity evolution.

the internal collapse as a rapid shortening of the cavity is a new unstable phenomenon.

### 3.2. Description of the internal reverse advance collapse

As mentioned above, the internal collapse is a particular phenomenon and should be given focus. The variation of the cavity length throughout the whole launching process is shown in Fig. 6. The process of the internal collapse process involves two different periods. In the first period, the length varies almost linearly. In the second period, the shortening process becomes faster first, and then the length variation becomes slower.

Observations of the cavity show that the shortening in the first period is similar to the shock propagation in the cavity, and a small

amount of free bubbles are generated after the collapse occurs at the closure of the cavity (as shown in Fig. 7(I)–(III)). In the second period, the cavity in the large region vanishes quickly, and a large amount of free bubbles are generated. The rebound is also observed after the collapse occurs at the closure of the main cavity. Observations of the collapse in the second period are more similar to the typical process of the collapse of the bubble cloud shed from the sheet cavity [37]. However, this internal collapse advances reversely and lasts for a longer time period, affects a larger region, and exerts a more significant impact on the projectile surface.

### 3.3. Influence of the internal collapse on the formation of the re-entry jet

The re-entry jet is one of the most important factors of cavitation instability. During the launching process, high-pressure pulses are generated by the internal collapse. Consequently, a large adverse pressure gradient is generated by the internal collapse, which induces the strong re-entry jet. The development of the re-entry jet is observed beginning from the internal collapse process (as shown in Fig. 8, with the red arrows pointing to the frontier of the re-entry jets). The motion of the re-entry jet front is approximately linear, so that the average velocity is calculated by linear fitting as 19.48 m/s, which is similar to the mean inflow velocity. Compared with the measurements of Callenaere et al. [24], in which the speed of the re-entry jet is about half of the mean inflow velocity, the re-entry jet is significantly strengthened by the internal collapse. Furthermore, this means that the instabilities of the evolution of the cavitation bubbles are also much aggravated.

## 4. Discussions on the mechanism

### 4.1. Analyses of the mechanism of the internal collapse

The cavitation number is usually considered to be the governing parameter of the cavity development. The mechanism of the

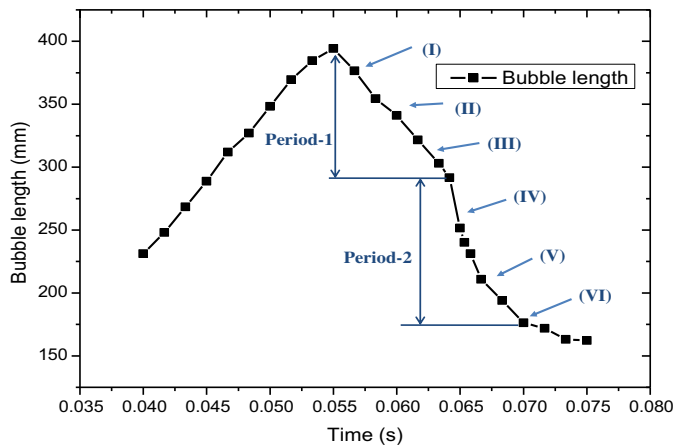


**Fig. 6.** Lengths of the main cavity in experimental results. The values of the length are calculated by pixel analysis. The measurement error is about 1 pixel, which is equal to 0.89 mm. The shortening process of the cavity involves two different periods according to the shortening rate. The Roman numerals represent the serial numbers of the pictures in Fig. 7.

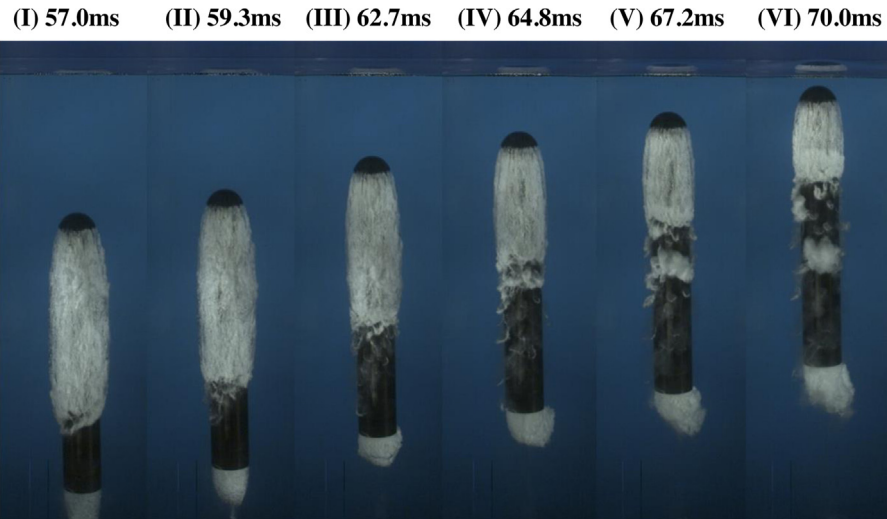


**Fig. 7.** Cavity evolutions in the fast shortening period (the serial numbers of the pictures are marked in Roman numerals in Fig. 6).

internal collapse is qualitatively analyzed based on the variation of the local cavitation number and the interfacial dynamic situation of the cavity. During the whole process, the local cavitation number at the head of the projectile can be calculated as  $\frac{p_{local}-p_v}{1/2\rho v^2}$  (as shown in Fig. 9), where  $p_{local}$  is the local hydrostatic pressure,  $p_v$  is the evaporation pressure,  $\rho$  is water density, and  $v$  is the instantaneous speed of the projectile.

In the acceleration process, the speed of the projectiles accelerates very fast in the tube, with the water depth declining quickly. The local cavitation number decreases significantly from several hundreds to approximately 0.16 (as shown in Fig. 9). Consequently, the main bubble is inceptioned from the shoulder and then grows quickly.

After the projectile runs out of the tube, its speed starts to decrease, inducing the local cavitation number to rise (as shown in Fig. 9). Correspondingly, deceleration forms additional body forces at the closure of the cavity, which in turn induce the pressure around the closure of the cavity to increase. As a result, the vapor at

the closure has a large condensable rate. The experimental results show that re-entry jets already form before the internal collapse occurs. Thus, the cavities at this time are thin and long between the re-entry jets and main flow and are suspended in a certain distance from the projectile surface (as shown in Fig. 10(a)).

The cavity boundary moves inward quickly given the pressure differences inside and outside. Furthermore, constrained by the projectile surface, the velocity directed to the wall is much larger than the velocity in the reverse direction. As a result, the liquid water layer continues to move toward and impact the wall as an internal collapse (as shown in Fig. 11).

Once the collapse occurs, high pressure is generated at the closure and is propagated to the leading edge as a shock (as shown in Fig. 10(b) and (c)). In addition, complex structures exist inside the cavity before the internal collapse, perhaps including the breakage in the thick region, which may cause the collapse to occur faster near the breaking region. When the collapse approaches the leading edge, condensation at the closure is much weakened by the

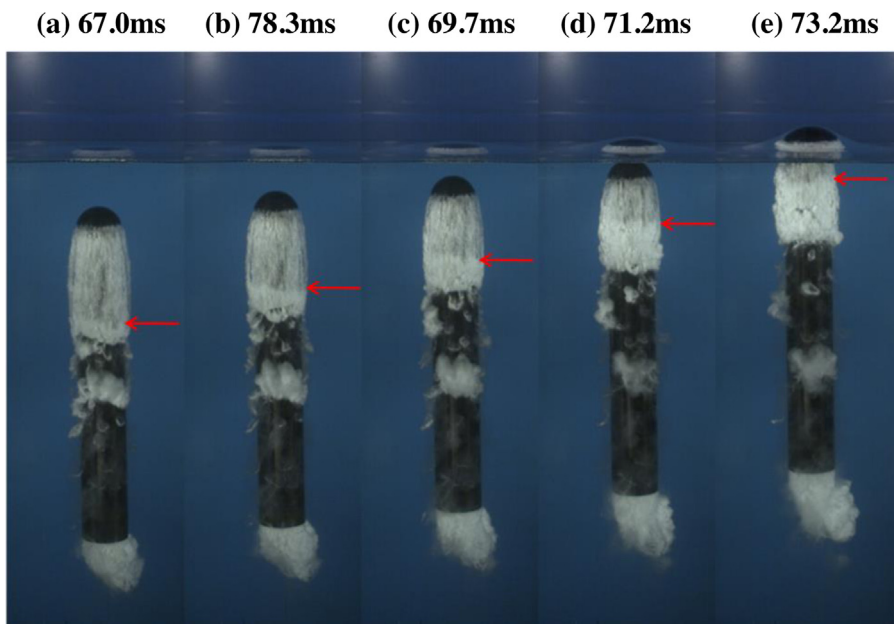


**Fig. 8.** Re-entry jet after the internal collapse (the front of the re-entry jet is shown as an interface between the bright and dark parts, marked by red arrows in each picture) (For interpretation of the references to color in this figure legend, the reader is referred to the web version of this article.).

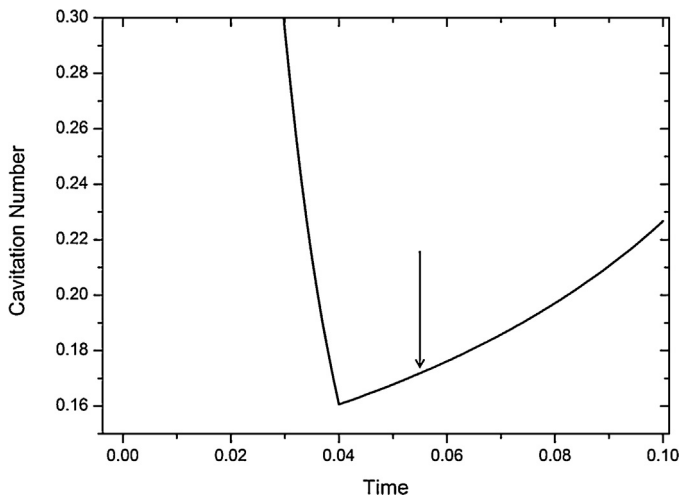


**Fig. 9.** Local cavitation number at the head of the projectile (the initial time of the internal collapse is indicated by the arrow).

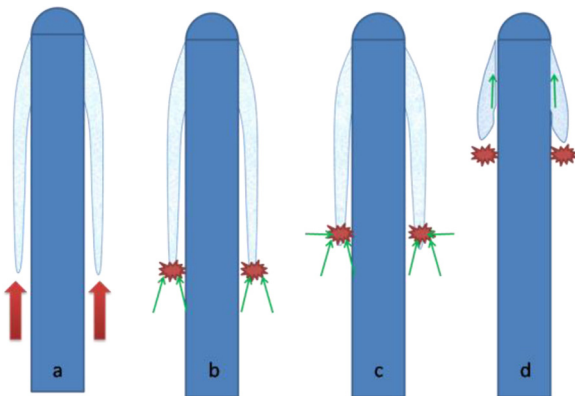


**Fig. 10.** Schematic of the dynamic analysis of the evolution of the cavity during the deceleration period. The strong body forces are shown as red arrows in (a), while the flow direction of liquid water is represented by green arrows in (b)–(d) (For interpretation of the references to color in this figure legend, the reader is referred to the web version of this article.).

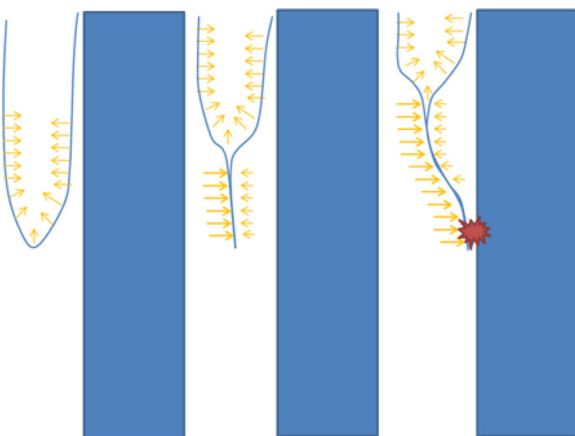


**Fig. 11.** Schematic of the motion of the cavity boundary near the collapse point at the closure of the cavity. The yellow arrows represent the directions of liquid water motion near the boundary (For interpretation of the references to color in this figure legend, the reader is referred to the web version of this article.).

low-pressure region around the projectile shoulder. Subsequently re-entry jets form as a result of the adverse pressure gradient, and the internal collapse finally terminates (as shown in Fig. 10(d)).

As indicated in the aforementioned analysis, the fast deceleration of the speed of the projectile is the main cause of the internal collapse. In addition, the cavity is very long, thin, and influenced by the fast acceleration, which induces the collapse to propagate from the trailing edge to the leading edge. Therefore, the present phenomenon is more unstable than other phenomena and is hardly observed in water tunnel tests.

#### 4.2. Parameter analysis of the deceleration

The influence of deceleration as the governing factor of the cavitating flow is studied by numerical simulation in this subsection. First, on the form of the motion of the acceleration–deceleration discussed in the present study, the governing parameters of bubble length are derived as follows:

$$L_b = f(t, \rho_w, v_{\max}, D, \mu_w, P_\infty - P_v, a_a, a_d) \quad (10)$$

where  $L_b$  is the length of the cavitation bubble,  $t$  is the time,  $\rho_w$  and  $\mu_w$  are the density and viscosity of water, respectively,  $D$  and  $v_{\max}$  are the diameter and the maximum speed of the projectile, respectively,  $P_\infty - P_v$  is the pressure difference between the reference and vaporization pressure, and  $a_a$  and  $a_d$  are the acceleration of the projectile in the accelerating and decelerating processes, respectively.

The equation above can be transformed into the following dimensionless form, if the density, velocity, and diameter are chosen as the basic quantities:

$$\frac{L_b}{D} = f\left(\frac{tD}{v_{\max}}; \frac{\rho_w v_{\max} D}{\mu_w}, \frac{P_\infty - P_v}{1/2 \rho_w v_{\max}^2}, \frac{a_a D}{v_{\max}}, \frac{a_d D}{v_{\max}}\right). \quad (11)$$

where  $\frac{tD}{v_{\max}}$  is the dimensionless time,  $\frac{\rho_w v_{\max} D}{\mu_w}$  is the Reynolds number,  $\frac{P_\infty - P_v}{1/2 \rho_w v_{\max}^2}$  is the cavitation number, and  $\frac{a_a D}{v_{\max}}$  and  $\frac{a_d D}{v_{\max}}$  are the dimensionless accelerations. If the process of the increase in velocity is fixed, the decelerating effect is controlled by the parameter  $\frac{a_d D}{v_{\max}}$ .

The basic numerical simulation of the cavitating flow in the decelerating process is performed using the speed curve in Fig. 2. The time sequences of the distributions of the pressure and water volume fractions are as shown in Fig. 12. When the speed of the projectile begins to decrease at 0.04 s, the growth of the cavitation bubble persists because of the inertia of the flow (as shown in Fig. 12(a)). At 0.05 s, the growth slows down, and the pressure starts to increase at the closure of the cavity (as shown in Fig. 12(b)). At 0.06 s, the cavity begins to collapse at the closure and advances upstream (as shown in Fig. 12(c)). The propagating velocity of collapse becomes fast, and the pressure becomes higher at the closure at 0.07 s (as shown in Fig. 12(d)). In proportion to the accumulation of the high pressure at the closure, the cavity collapses as a local bubble cloud, inducing the velocity of the shrinking of the bubble to suddenly quicken at 0.08 s (as shown in Fig. 12(e)).

Detailed flow fields in collapse regions are shown in Fig. 13. There are flow stream with velocity pointing to the wall which are formed after the condensation process in the trailing area of the cavity (as shown in Fig. 13(b) and (d)). Strong collapse pressure is generated (as shown in Fig. 13(a) and (c)) by the impact of liquid water. Flow characteristics indicated in Fig. 13 are similar with those schematics in Fig. 11, which can validate relevant mechanism analysis.

Strong adverse pressure gradient is formed by the collapse pressure at the cavity closure and generates the re-entry jet as shown in Fig. 14. Consequently the liquid water is carried by the re-entry jet on the bottom of the cavity to the leading edge. And the vapor region

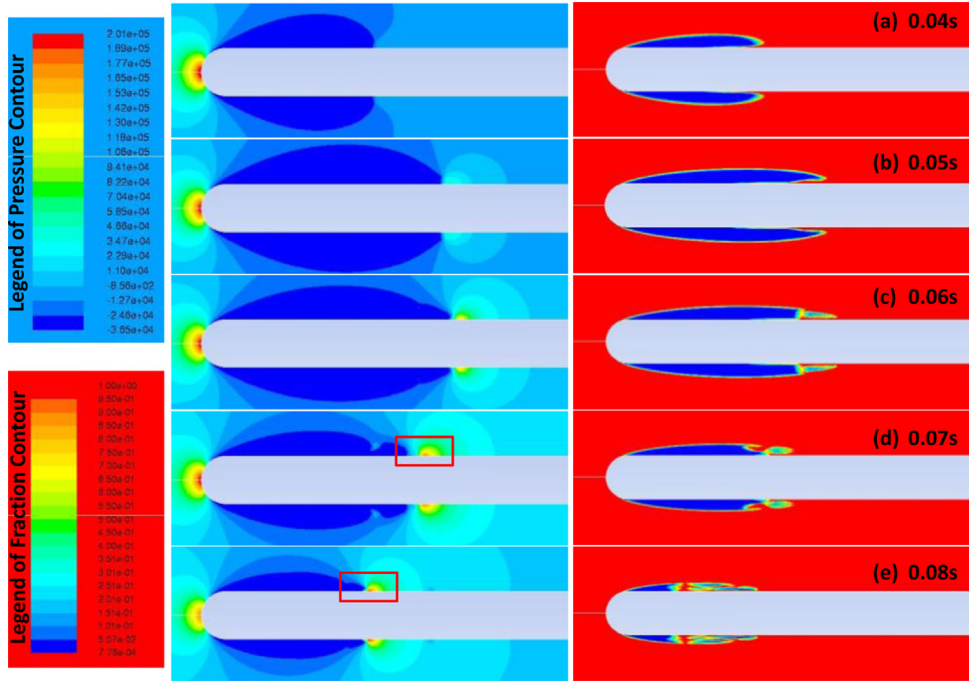


**Fig. 12.** Time sequences of the pressure (left) and water volume fractions (right) during the internal collapse stage in the numerical results. Collapse regions are surrounded in red rectangles (For interpretation of the references to color in this figure legend, the reader is referred to the web version of this article.).

is separated from the wall surface, which induces the subsequent collapse to happen easily. The shape and characteristics shown in Fig. 14 are similar with those schematics shown in Fig. 10.

Various cavitating flows are also simulated by amplifying the deceleration. The variations in cavity lengths are as shown in Fig. 15, with three different amplification factors. The varying tendencies of the cavity lengths in numerical and experimental results coincide with one another, and their magnitudes are similar. In proportion to the enlargement of the deceleration, the cavities shorten more quickly.

Certain differences in the variation in the cavity length continue to exist between the experimental and numerical results, for example, the computed decrease rate of cavity length is much smaller than in the experiment, which embody some of the defects of the numerical model. For example, the free surface and 3D effects are unconsidered, and the accelerating process is unknown and is an uncertain factor, thereby resulting in the difference in maximum cavity lengths. Moreover, it is interesting to notice that the computed decrease rate of the cavity length during “period-1” is almost proportional to the deceleration rate, while that during

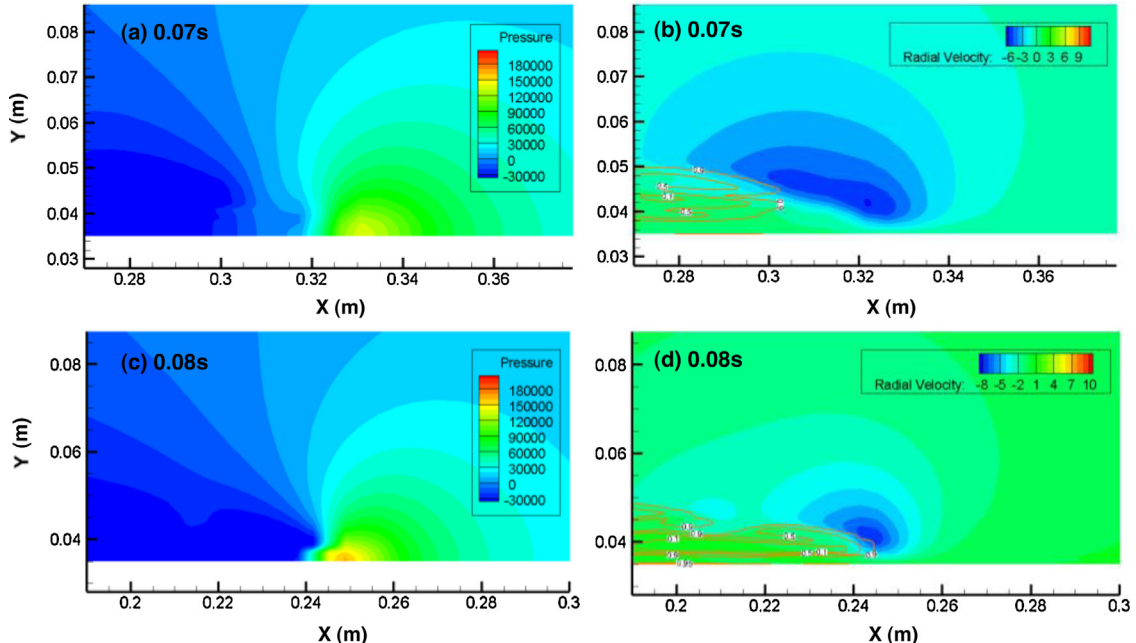


**Fig. 13.** Flow field near collapse regions at cavity closure which are surrounded by red rectangles in Fig. 12. Flood contours represent pressure fields in left views. Line contours in right views show water volume fractions with levels of 0.1, 0.5 and 0.9. Flood contours show radial velocity in the views in which the blue color represents large velocity pointing to the wall surface (For interpretation of the references to color in this figure legend, the reader is referred to the web version of this article.).

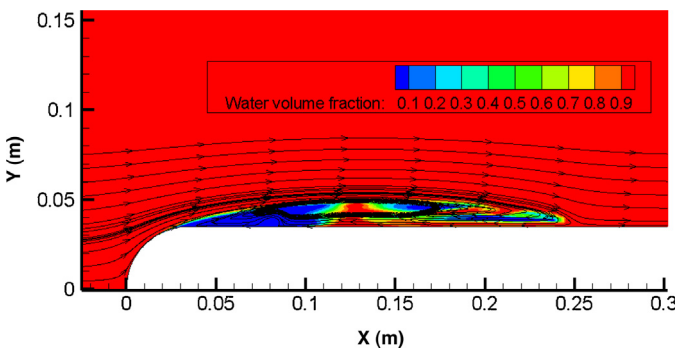


**Fig. 14.** Re-entry jets in the cavity represented by streamlines at time = 0.08 s. The flood contour represents the water volume fraction. The re-entry jet is generated at the cavity closure and flows to the leading edge with entrainment of liquid water.

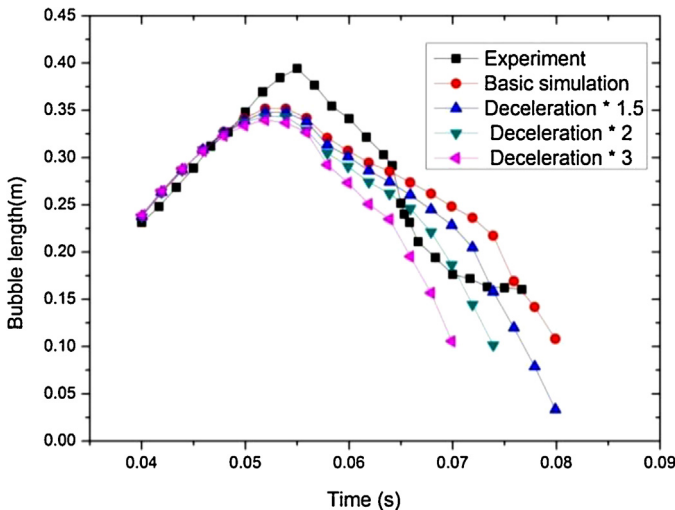


**Fig. 15.** Variation in the cavity lengths in the experimental and numerical results. Various cavity evolutions are obtained by changing the deceleration rate, while maintaining the acceleration rate under different numerical simulation conditions.

“period-2” is almost constant and independent of the deceleration rate. This fact may suggest that cavity collapse during period-1 is due to the increase of the cavitation number and deceleration, and that during period-2 is due to the instability of cavity itself.

## 5. Conclusions

In a typical underwater launch experiment, a special internal collapse was observed as a propagation process from the trailing edge to the leading edge, and relevant cavity evolutions and mechanisms were analyzed. Our results indicate the following:

During the deceleration stage, cavitation bubbles collapse at the closure and advance upstream. This is significantly different from the common collapse of shedding cavitation clouds.

For the dynamic mechanism, high pressure is generated by the additional body force induced by the fast deceleration. Consequently, internal collapse occurs and produces high-impact pressure. The major reasons for this internal collapse are the fast acceleration and deceleration of the projectile speed.

Induced by the pressure of the internal collapse, the strong re-entry jet forms, and the instabilities in the evolution of the cavitation bubbles are aggravated.

Numerical simulations are performed on the decelerating effect on the cavity evolution. The results indicate that the pressure increase is a critical factor that results in the nonlinear change in

the cavity length. In proportion to the enlargement of deceleration, the cavities shorten more quickly.

Speed variation may be an important issue in the cavitating flow of the application of high-speed underwater vehicle. In particular, deceleration can lead to the aggravation of cavitation instability and should be studied further. To obtain more accurate results, more precise experimental and numerical approaches are required in the future.

## Acknowledgements

The authors are grateful to National Natural Science Foundation of China through grant numbers 11202215 & 11332011 and the Youth Innovation Promotion Association of CAS (2015015).

## References

- [1] Brennen CE. Cavitation and bubble dynamics. USA: Oxford University Press; 1995.
- [2] Brenner MP, Hilgenfeldt S, Lohse D. Single-bubble sonoluminescence. *Rev Mod Phys* 2002;74(2):425–84.
- [3] Lauterborn W, Kurz T. Physics of bubble oscillations. *Rep Prog Phys* 2010;73(10):106501.
- [4] Schanz D, Metten B, Kurz T, Lauterborn W. Molecular dynamics simulations of cavitation bubble collapse and sonoluminescence. *New J Phys* 2012;14(11):113019.
- [5] Lind SJ, Phillips TN. Spherical bubble collapse in viscoelastic fluids. *J Non-Newton Fluid Mech* 2010;165(1):56–64.
- [6] Plesset MS, Chapman RB. Collapse of an initially spherical vapour cavity in the neighbourhood of a solid boundary. *J Fluid Mech* 1971;47(2):283–90.
- [7] Plesset MS, Prosperetti A. Bubble dynamics and cavitation. *Annu Rev Fluid Mech* 1977;9(1):145–85.
- [8] Johnsen E, Colonius T. Numerical simulations of non-spherical bubble collapse. *J Fluid Mech* 2009;629:231–62.
- [9] Wang QX. Non-spherical bubble dynamics of underwater explosions in a compressible fluid. *Phys Fluids* 2013;25(7):072104.
- [10] Seo JH, Lele SK, Tryggvason G. Investigation and modeling of bubble–bubble interaction effect in homogeneous bubbly flows. *Phys Fluids* 2010;22:063302.
- [11] Bremond N, Arora M, Ohl CD, Lohse D. Controlled multibubble surface cavitation. *Phys Rev Lett* 2006;96(22):224501.
- [12] Lauer E, Hu XY, Hückel S, Adams NA. Numerical investigation of collapsing cavity arrays. *Phys Fluids* 2012;24(5):052104.
- [13] Pelekanis NA, Gaki A, Doinikov A, Tsamopoulos JA. Secondary Bjerknes forces between two bubbles and the phenomenon of acoustic streamers. *J Fluid Mech* 2004;500:313–47.
- [14] Quinto-Su PA, Ohl CD. Interaction between two laser-induced cavitation bubbles in a quasi-two-dimensional geometry. *J Fluid Mech* 2009;633:425–35.
- [15] Han B, Köhler K, Jungnickel K, Mettina R, Lauterborna W, Vogela A. Dynamics of laser-induced bubble pairs. *J Fluid Mech* 2015;771:706–42.
- [16] Tiwari A, Pantano C, Freund JB. Growth-and-collapse dynamics of small bubble clusters near a wall. *J Fluid Mech* 2015;775:1–23.
- [17] Rossinelli D, Hejazialhosseini B, Hadjidoukas P, Bekas C, Curioni A, Bertsch A, et al. 11 PFLOP/s simulations of cloud cavitation collapse. High Performance Computing, Networking, Storage and Analysis (SC). In: 2013 International Conference for IEEE. 2013.
- [18] Puent GF, Bonetto FJ. Proposed method to estimate the liquid-vapor accommodation coefficient based on experimental sonoluminescence data. *Phys Rev E* 2005;71(5):056309.
- [19] Wang YC, Brennen CE. Numerical computation of shock waves in a spherical cloud of cavitation bubbles. *J Fluids Eng* 1999;121(4):872–80.
- [20] Fuster D, Colonius T. Modelling bubble clusters in compressible liquids. *J Fluid Mech* 2011;688:352–89.
- [21] Wang YW, Liao LJ, Du TZ, Huang CG, Liu YB, Fang X, et al. A study on the collapse of cavitation bubbles surrounding the underwater-launched projectile and its fluid-structure coupling effects. *Ocean Eng* 2014;228–36.
- [22] Liu Y, Zhang A, Tian Z. Approximation of underwater explosion bubble by singularities based on BEM. *Ocean Eng* 2014;75:46–52.
- [23] Cui P, Zhang A, Wang S, Wang Q. Experimental investigation of bubble dynamics near the bilge with a circular opening. *Appl Ocean Res* 2013;41:65–75.
- [24] Callewaert M, Franc JP, Michel JM, Riondet M. The cavitation instability induced by the development of a re-entrant jet. *J Fluid Mech* 2001;444:223–56.
- [25] Le Q, Franc J, Michel J. Partial cavities: pressure pulse distribution around cavity closure. *J Fluids Eng* 1993;115(2):249–54.
- [26] Reisman GE, Wang Y, Brennen CE. Observations of shock waves in cloud cavitation. *J Fluid Mech* 1998;355(1):255–83.
- [27] Saito Y, Takami R, Nakamori I, Ikoaghi T. Numerical analysis of unsteady behavior of cloud cavitation around a naca0015 foil. *Comput Mech* 2007;40(1):85–96.
- [28] Konno A, Kato H, Yamaguchi H, Maeda M. On the collapsing behavior of cavitation bubble clusters. *JSME Int J Ser B* 2002;45(3):631–7.
- [29] Saito Y, Sato K. Cavitation bubble collapse and impact in the wake of a circular cylinder. In: Fifth International Symposium on Cavitation (CAV2003). 2003.

- [30] Li KB, Wang AW, Mao LW, Fu SQ. Shapes and memory effects of natural supercavitation of navigating bodies with variable speeds. *J Huazhong Univ Sci Technol (Nat Sci Edit)* 2013;41(6):94–8.
- [31] Yang HL, Zhang JZ, Zhao CB, Huang WH. Analyse and prediction of supercavities' shape of cone cavitator with variable motion. *J Hydron – Ser A* 2007;22(1):53–60.
- [32] Wang HB, Zhang JZ, Wang C, Wei YJ, Jia LP. Numerical simulation of acceleration effect on natural supercavity. *Eng Mech* 2007;24(1):18–22.
- [33] Chen Y, Lu CJ, Chen X, Cao JY. Numerical investigation on the cavitation collapse regime around the submerged vehicles navigating with deceleration. *Eur J Mech – B/Fluids* 2015;49:153–70.
- [34] Zwart PJ, Gerber AG, Belarmi T. A two-phase flow model for predicting cavitation dynamics. In: Fifth International Conference on Multiphase Flow. 2004.
- [35] Dular M, Bachert R, Stoffel B, Širok B. Experimental evaluation of numerical simulation of cavitating flow around hydrofoil. *Eur J Mech – B/Fluids* 2005;24(4):522–38.
- [36] Wang YW, Huang CG, Du TZ, Liu WW. Numerical simulation of a submerged body exiting from water with an attack angle. *Chin J Hydron* 2011;26(1):48–57.
- [37] Yu X, Huang C, Du T, Liao LJ, Wu XC, Zheng Z, et al. Study of characteristics of cloud cavity around axisymmetric projectile by large eddy simulation. *J Fluids Eng* 2014;136(5):051303.